

Co-current flow effects on a rising Taylor bubble

Shaoping Quan

Institute of High Performance Computing, 1 Fusionopolis Way, 16-16 Connexis, Singapore 138632, Singapore

ARTICLE INFO

Article history:

Received 11 November 2010

Received in revised form 13 April 2011

Accepted 21 April 2011

Available online 28 April 2011

Keywords:

Taylor bubble

Archimedes number

Co-current

Upward

Downward

Velocity ratio

Front tracking

Wake

Vortex rings

Thin film

Wall shear stress

ABSTRACT

The effects of co-current flows on a rising Taylor bubble are systematically investigated by a front tracking method coupled with a finite difference scheme based on a projection approach. Both the upward (the co-current flows the same direction as the buoyancy force) and the downward (the co-current moves in the opposite direction of the buoyancy force) co-currents are examined. It is found that the upward co-current tends to elongate the bubble, while the downward co-current makes the bubble fatter and shorter. For large N_f (the inverse viscosity number), the upward co-current also elongates the skirted tail and makes the tail oscillate, while the downward co-current shortens the tail and even changes a dimpled bottom to a round shape. The upward co-current promotes the separation at the tail, while the downward co-current suppresses the separation. The terminal velocity of the Taylor bubble rising in a moving flow is a linear combination of the mean velocity (U_c) of the co-current and the terminal velocity (U_0) of the bubble rising in the stagnant liquid, and the constant is around 2 which agrees with the literature. The wake length is linearly proportional to the velocity ratio (U_c/U_0). The co-currents affect the distribution of the wall shear stresses near the bubble, but not the maximum.

© 2011 Elsevier Ltd. All rights reserved.

1. Introduction

The dynamics of Taylor bubbles rising through vertical tubes filled with another viscous fluids has been an interesting subject for decades due to their wide existence in many engineering applications and real life, such as: nuclear reactors, oil–gas pipelines, steam boilers, heat exchangers, and blood flows. Taylor bubbles usually have a rounded leading edge, a long cylindrical middle part, and a trailing edge with either rounded, or flattened, or dimpled shape. The length of Taylor bubbles can be as long as several diameters of the tube, and they almost fully occupy the cross-section of the tube, and thus a thin film appears between the bubbles and the tube inner walls.

The literature on Taylor gas-bubbles rising in initially stagnant fluids is abundant and the pioneer research was performed by Dumitrescu (1943) and Davies and Taylor (1950). They theoretically found that the rising velocity of a Taylor bubble in the inviscid limit is: $U_0 = \alpha\sqrt{gD}$, where g is gravitational acceleration, D denotes the tube diameter, and the value of the coefficient α is around 0.33–0.35. This correlation has been confirmed by experimental observations (Campos and Guedes de Carvalho, 1988; Polonsky et al., 1999). The motion of Taylor bubbles was reviewed by Clift et al. (1978) and Fabre and Liné (1992) in great detail. The dynamics of the Taylor gas bubble rising in a stagnant viscous fluid

is governed by a group of non-dimensional numbers, namely: the Eötvös number (Eo), the Archimedes number (Ar) or the inverse viscosity number (N_f), the Reynolds number (Re_T), the Weber number (We_T), the Froude number (Fr), the density ratio (η), and the viscosity ratio (λ), and these numbers are defined as:

$$Eo = \frac{(\rho_s - \rho_b)gD^2}{\sigma}; \quad Ar = N_f^2 = \frac{\rho_s(\rho_s - \rho_b)gD^3}{\mu_f^2}; \quad Re_T = \frac{\rho_s U_0 D}{\mu_s};$$

$$We_T = \frac{\rho_s U_0^2 D}{\sigma}; \quad Fr = \frac{U_0}{(gD)^{1/2}}; \quad \eta = \frac{\rho_s}{\rho_b}; \quad \lambda = \frac{\mu_s}{\mu_b}.$$

In these definitions, the viscosities and the densities of the suspending fluid and the bubble are denoted by μ_s and μ_b , ρ_s and ρ_b , respectively; g is the gravitational acceleration; σ stands for the surface tension coefficient and is assumed constant; U_0 is the terminal velocity of the bubble. Recently, universal correlations for the rising velocity of Taylor bubbles in stagnant fluids contained in circular tubes were proposed by Viana et al. (2003) by analyzing hundreds experimental data from the literature. Using a viscous potential flow model, Mandal et al. (2007) demonstrated that the rising velocity of liquid Taylor bubbles is also related to the shape of the nose. Besides the terminal velocity, the fluid field and the bubble shape are also of great interest of research (Campos and Guedes de Carvalho, 1988; van Hout et al., 2002; Bugg and Saad, 2002; Nogueira et al., 2006a; Nogueira et al., 2006b).

E-mail address: quansp@ihpc.a-star.edu.sg

In cases where the suspending fluid initially flows instead of being stagnant, the dynamics of Taylor bubbles is more complex, while the literature is rather limited. Nicklin et al. (1962) proposed that the terminal velocity of a Taylor bubble rising in a moving fluid (U_B) is a linear combination of the mean velocity of the co-current (U_C) and the rising velocity in the stagnant liquid (U_0), i.e.

$$U_B = CU_C + U_0 = CU_C + \alpha\sqrt{gD} \quad (1)$$

where U_C denotes the mean velocity of the co-current flow, and C is a constant. It was found that C takes value around 1.2 for turbulent flows, and for laminar it is around 2 (Nicklin et al., 1962; Collins et al., 1978; Grace and Clift, 1979; Bendiksen, 1985). Polonsky et al. (1999) experimentally studied the relation, and they found that the value of C is depended on the co-current velocity. Nogueira et al. (2006a,b) performed experiments on the detailed velocity field around a Taylor bubble rising through vertical tubes filled with upward flowing Newtonian liquids, and they demonstrated that the wake length increases linearly with a Reynolds number based on the superficial liquid velocity relative to the bubble. Pinto et al. (2000) investigated the transition in the Taylor bubble velocity in vertical upward co-currenting liquids, and they reported that the coefficient C is a function of the Reynolds number, the Weber number, and U_C/U_0 .

Numerical modeling serves an alternative to explore the dynamics of Taylor bubbles in initially stagnant fluids, for example (Mao and Dukler, 1991; Bugg et al., 1998; Ndinisa et al., 2005; Taha and Cui, 2006; Akbar and Ghiaasiaan, 2006). For Taylor bubbles rising with co-currents, Lu and Prosperetti (2009) simulated Taylor bubbles rising in a vertical tube filled with stagnant, upward or downward flowing liquids by a finite volume method coupled with marker points to track the interface.

The objective of this work is to systematically investigate the co-current (including both upward and downward flows) effects on a rising Taylor bubble. A front tracking scheme coupled with finite difference method is employed as this scheme has been extensively validated for the simulations for bubble rising (Mukundakrishnan et al., 2007) and especially for a Taylor bubble rising in a stagnant fluid (Kang et al., 2010). In the front tracking scheme, the two-fluid flow (including the gas inside the bubble and the suspending liquid) is solved, and thus both the velocity fields inside and outside the bubble can be revealed. The effects of the co-currents on the terminal velocity and the overall shape of the bubble are studied. The detailed investigations of the shape in the nose and tail regions, the velocity inside bubble and in the thin film region, and the wall shear stresses are presented. Correlations between the bubble rising velocity and the mean velocity of the suspending flow are obtained and compared with the published results. A correlation between the wake length and the co-current velocity is also proposed.

2. Problem setup and numerical methods

Fig. 1 displays the computational domain and the initial bubble shape for the simulations. The problem is assumed rotational symmetry (or axi-symmetry), and the axis of the symmetry is denoted by the dash-dot-dot line. Therefore, all the simulations are performed in a cylinder coordinate system (r, z). The cylindrical tube has an inner radius of $R_0 = 1.6$ cm and a length of $30R_0$, and the side wall of the tube is denoted by the thick line. The density and viscosity of the bubble are ρ_b and μ_b , and ρ_s and μ_s for the suspending fluid. The two fluids are assumed incompressible and immiscible. The gravitational force is downward. The initial bubble has a shape of a cylinder with two hemispheres at the two ends. The radius of the middle section is r_0 , which is $0.84R_0$, and the length of the initial bubble is $4r_0$. As both the upward and downward co-currents

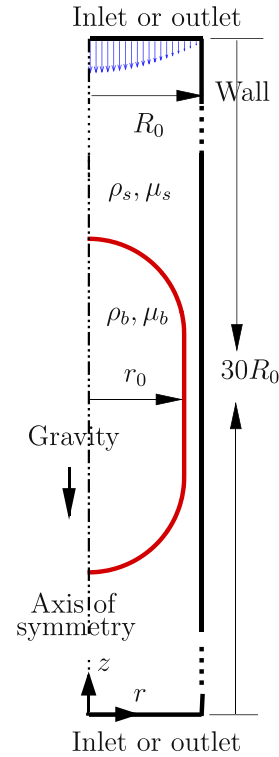


Fig. 1. Sketch of a Taylor bubble (the red thick line) rising in a cylindrical tube filled with a co-current fluid. The co-current either flows downwards or upwards with a parabolic velocity distribution. (For interpretation of the references to color in this figure legend, the reader is referred to the web version of this article.)

are of the interest of study, the bottom and top of the simulation domain can either be outlet or inlet. The velocity profile at the inlet of the co-current is parabolic, i.e. $u_z^{inlet} = U_C(1 - r^2)$ with r being non-dimensional radius, to mimic the fully-developed pressure-driven Poiseuille flow in a cylindrical tube. As the suspending fluid is moving, one extra governing non-dimensional number is introduced, i.e. the velocity ratio (U_C/U_0). Then, the Reynolds number (Re_{U_B}) and Weber number (We_{U_B}) are based on the terminal velocity of the Taylor bubble in the moving fluid, U_B .

The numerical scheme solves the Navier–Stokes equations by a finite difference method with a projection scheme (Bell and Marcus, 1992), and the flow is assumed to be laminar. The interface is located by the front tracking scheme (see Tryggvason et al. (2001) for a great review of the method and Esmaeili and Tryggvason (1998, 1999, 2005) for the applications). The detail of the current implementation of the method for bubble rising including the validations can be found in Kang et al. (2010), Mukundakrishnan et al. (2007), and here only a brief summary is given. In the projection approach, first, an intermediate velocity is obtained by a semi-viscous procedure in which a one-time-step lagged pressure is used. This intermediate velocity, of course, does not satisfy the continuity equation. Therefore, the intermediate velocity field is then projected onto discretely divergence-free vector fields. The Crank–Nicholson method is employed for the time integration. The interface (or front) moves in a trapezoidal mode by the velocity interpolated from the neighboring fixed grids. The surface tension forces which are calculated on the interface and then are distributed to the surrounding grids using a δ function (Griffith and Peskin, 2005) in a density-weighted manner. The viscosity is calculated by a harmonic mean method, and similar schemes can be found in Gunsing (2004) and Prosperetti and Tryggvason (2007). The numerical method has been extensively validated against a number of experiments for a bubble and a Taylor bubble

independent of the density ratio once it is sufficiently small. Using a volume of fluid approach, Chen et al. (1999) demonstrated that the shapes of the simulated bubbles with density ratios of 1000 and 80 are similar.

3. Results and discussion

Fig. 2 shows a typical simulation result for $N_f = 200$ and $U_C/U_0 = -0.13$. The bubble shape is represented as the thick line in the middle of computational domain. The axis of symmetry is

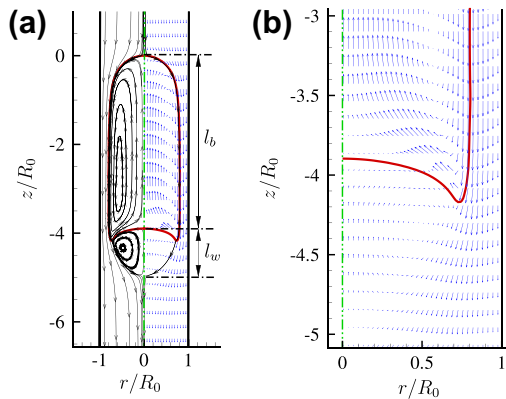


Fig. 2. Presentation of the shape and velocity field of a typical simulation. $\mu_s = 1.09 \text{ g/(cm s)}$, $N_f = \sqrt{Ar} = 200$, $U_C/U_0 = -0.13$.

located at $r/R_0 = 0$, and is denoted by the dash-dot-dot line. The cylinder walls are denoted by the two thick vertical lines at r/R_0 of 1 and -1 . The fluid velocity vectors for both the bubble and the suspending phases are displayed on the right-hand side, while the corresponding stream lines are shown on the left-hand side to observe the wake flow structure. The reference frame moves with the bubble nose. The wake length, l_w , is defined as the length on the axis of symmetry from the bubble bottom to the closing point of the wake vortex ring. To quantitatively compare the bubble length, a bubble body length (l_b) is defined as the distance on the symmetric axis from the nose to the bottom. To clearly observe the velocity and tail shape, an enlarged view of the tail region is displayed in Fig. 2b. From this enlarged view, it is noted that there are at least 12 grids in the thin film region by considering that the velocity vectors are plotted by skipping every other point. The simulated wake length is compared with the empirical correlation by Campos and Guedes de Carvalho (1988) for $U_C/U_0 = 0$. The correlation reads $l_w = 0.6 + 2.44 \times 10^{-3} N_f$. For $N_f = 291, 200$, and 109 , the correlation gives l_w of 1.31, 1.09, 0.87, and our simulations predict l_w of 1.86, 1.31, and 0.69, respectively. The way of measuring the wake length is believed to be a major factor for the difference. In the simulations, the wake length is measured from the highest point of the concave surface, while it is a challenge to exactly measure the length of the dimpled region in the experiments.

3.1. Bubble shape and velocity field

Fig. 3 shows co-current effects on both the overall shape of the Taylor bubble and velocity field for different viscosities of the

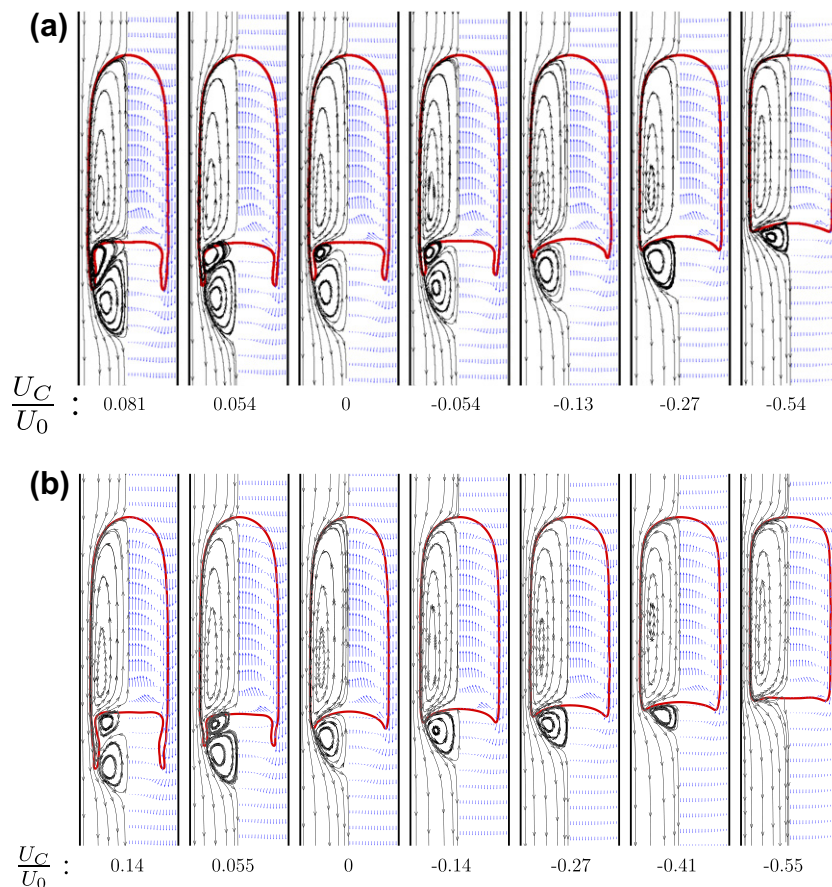


Fig. 3. Co-current effects on the overall shape and velocity field of a Taylor bubble rising in a fluid with various viscosities. $Eo = 248$, $\lambda = \eta = 100$. (a) $\mu_s = 0.75 \text{ g/(cm s)}$, $N_f = \sqrt{Ar} = 291$; (b) $\mu_s = 1.09 \text{ g/(cm s)}$, $N_f = \sqrt{Ar} = 200$; (c) $\mu_s = 2 \text{ g/(cm s)}$, $N_f = \sqrt{Ar} = 109$; (d) $\mu_s = 10 \text{ g/(cm s)}$, $N_f = \sqrt{Ar} = 22$. The minus sign in the flow ratio indicates that the co-current moves downward, which is opposite to the buoyancy force.

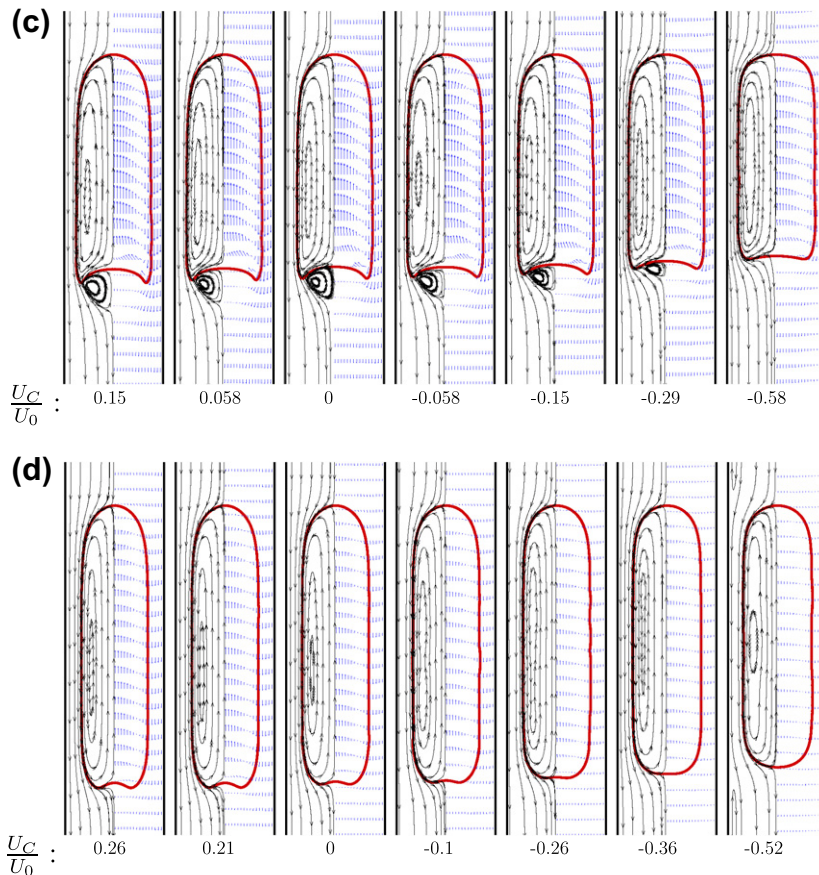


Fig. 3 (continued)

suspending fluids. The noses of all the Taylor bubbles are aligned to $z/R_0 = 0$ (Fig. 2) to facilitate the comparison of the lengths of the bubbles. The length (l_b) of the main body of each bubble increases with the decrease of N_f , which indicates that the viscous force tends to elongate the bubble. As each bubble has the same volume, the bubble becomes thinner, which results in a wider thin film region between the bubble and the tube wall. The relationship between the width of the thin film and the Archimedes number (Ar) was reported in the early work (Kang et al., 2010). For the cases with $N_f = 109$ and 22, the bubble major body becomes shorter with the decrease of U_c/U_0 . However, for $N_f = 291$ and 200 with the upward co-current (i.e. the cases in Fig. 3a and b where $U_c/U_0 > 0$), the length of the major body does not follow this trend due to the long tail at the bottom of the bubble which occupies a significant portion of the total mass of the bubble. Of course, to conserve mass the bubble becomes fatter with the decrease of the velocity ratio and this can be clearly observed in the figure, especially for the three cases with smaller N_f . To quantitatively compare the body length and the width of the liquid film, l_b and w_{tf} are listed in Table 1. From the table, it is clear that for each N_f case, the main trend of the bubble body length is that it decreases with the reduction of U_c/U_0 with a maximum decrease around 10%. However, the thin film width increases with the decrease of the velocity ratio, and the maximum variation is about 20% with $N_f = 291$ being the largest difference.

The co-current flow also influences the shape of the nose. Use Fig. 3, we note that the nose of the bubble for the smallest U_c/U_0 (i.e. the largest downward co-current rate) of cases with $N_f = 291$, 200 and 109 is blunter than the corresponding case with no co-current flow. To clearly examine the co-current effects on the nose shape, enlarged views of the bubble nose are plotted in Fig. 4 for

$N_f = 291$, 109 and 22, where only five velocity ratios are displayed. Compared to the nose with no co-current, the upward co-current makes the nose sharper, while the downward co-current makes the nose obtuse. As the co-current is a fully-developed pressure-driven Poiseuille flow, for the downward co-current, the pressure gradient slows down the upward motion induced by the buoyancy forces, and pushes down the region of the nose near the axis of symmetry harder than elsewhere because the pressure gradient at this region is almost perpendicular to the interface, while for anywhere else, only a fraction of pressure gradient is perpendicular to the interface there. This blunt nose also increases the drag coefficient of the rising Taylor bubble. For the upward co-current, the pressure gradient acts at the same direction as the bubble rising, and thus the bubble is accelerated. A sharper nose helps to reduce the drag forces. It is noted that Dumitrescu (1943) derived a Taylor bubble shape based on potential flow assumption for air–water system and they reported the non-dimensional geometry of the bubble is similar. However, our numerical simulation demonstrated that the bubble shape depends not only on the N_f but also on the co-current flow rate, which agrees with the experimental observation by Nogueira et al. (2006b). Using numerical simulations, Lu and Prosperetti (2009) also reported that upward co-current tends to make the nose of Taylor bubbles more pointed. For a gas bubble in an axisymmetric shear flow, Takagi et al. (1994) pointed out that the nose shape of the bubble is also affected by the external flows.

Compared to the effects on the shape of the nose, the co-current affects the tail of the Taylor bubble in a more significant way. Enlarged views of the tail region for $N_f = 291$, 200, and 22 are displayed on the right-hand of Fig. 4. For the lowest viscosity case ($N_f = 291$) with no co-current, the bubble has a skirted tail, and this

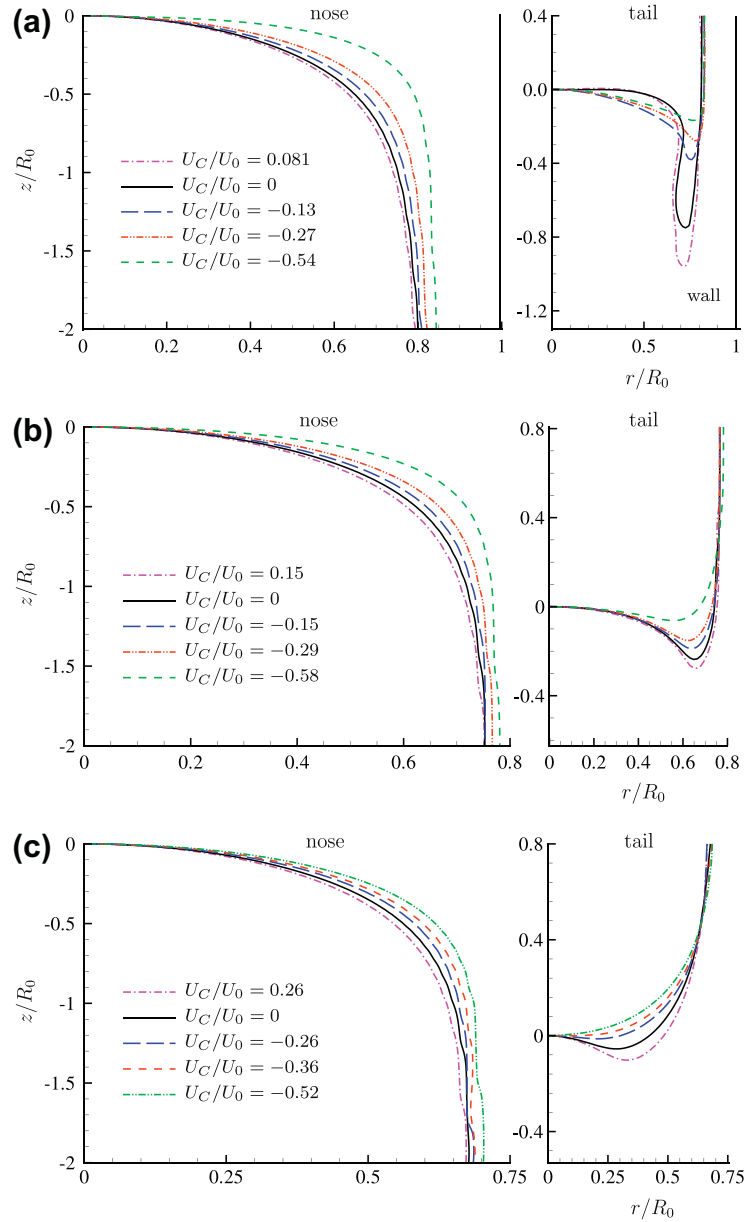


Fig. 4. Enlarged view of the nose and tail regions for three cases. (a) $N_f = 291$, (b) $N_f = 109$ and (c) $N_f = 22$. The negative sign in U_C/U_0 indicates that the co-current flows opposite to the rising direction of the bubble by buoyancy.

tail is wavy. With the increase of the upward flow rate, the tail becomes more elongated and wavier. The Weber numbers based on the bubble terminal velocity for the two upward co-currents are 29.6 and 26.1, which are larger than $(We_{U_B}) = 22.6$ for the case with no current flow (see Table 1). A larger (We_{U_B}) indicates that the interface is more easily deformed. However, with the increase of the downward flow rate, the bubble tail is continuously shortened and changes from a skirted shape to a dimpled one (especially for $U_C/U_0 = -0.54$). The downward pressure gradient slows down the bubble rising, and thus results in a smaller (We_{U_B}) . For $U_C/U_0 = -0.54$, the bubble has a $(We_{U_B}) = 0.2$, which indicates that the surface tension forces dominate and thus the bubble is more difficult to deform from its spherical shape. The variation of the tail shapes for $(N_f) = 200$ is very similar to the one with $N_f = 291$, except that the tail is just slightly skirted for $U_C/U_0 = 0$ (see Fig. 3). However, for $N_f = 109$, the change in the tail shapes is more moderate compared to the cases with $N_f = 291$ and 200. From the enlarged view of the tail regions in Fig. 4b, it is observed that the

concavity of the dimple becomes smaller with the decrease of U_C/U_0 , and the maximum curvature in the tail region also decreases. This trend can be explained by the reduction of the Weber number based on the terminal velocity. For $N_f = 22$, it is interesting to see that with the decrease of the velocity ratio, the bottom of the bubble become less concave, and for $U_C/U_0 = -0.36$ the bottom is flattened, and even for $U_C/U_0 = -0.52$, the bottom becomes convex and is almost round.

The co-current effects on the vortices in the domain are more interesting (see Fig. 3). Inside the Taylor bubbles, there is only one vortex ring, while this vortex ring changes its shape with the co-current to accommodate the geometry of the bubble. It should be noted that as the simulation is performed in the cylindrical coordinate system, the vortices observed in Fig. 3 are vortex rings. The effects on the vortices in the closed-wake are more complex. For the smallest viscosity case, there are two vortex rings with opposite circulating directions in the wake for the stagnant fluid case. With the increase of the downward co-current speed, there

is only one vortex ring left, and the length of the closed-wake decreases, and so does the length of the vortex rings. However, the number of the vortex rings remains two as the co-current speed ascends, while the size of the vortex nearer to the bubble bottom increases. For the case with $N_f = 200$, at the stagnant suspending fluid scenario, there is only one closed-wake vortex ring, and with the increase of the downward flow speed the size shrinks until $U_c/U_0 = -0.41$. For $U_c/U_0 = -0.55$, there is no vortex observed in the wake. However, the number of the vortex rings increases to two as the upward surrounding flow moves faster, and these two vortex rings rotate in opposite directions. For $N_f = 109$, the size of the wake vortex ring decreases with U_c/U_0 , and the vortex disappears at $U_c/U_0 = -0.58$. For the most viscous case in Fig. 3, i.e. $N_f = 22$, there is no wake vortex observed for all the scenarios, however, there is a side vortex observed at $U_c/U_0 = -0.52$ with a clockwise circulation. This side vortex was also reported by Lu and Prosperetti (2009) for Taylor bubbles rising in a co-current system. At this scenario, the downward co-current is strong enough to offset the flow in some region induced by the buoyancy forces in the surrounding phase, and thus stagnant points occur near the bubble and the tube wall. The existence of stagnant points in flows is a key factor for the vortex (Taylor, 1961). Similar vortex in the surrounding flow was reported in the work by Feng (2009) for a long gas bubble in a tube with a moving liquid.

To quantitatively investigate the co-current effects on the size of the close wake, the wake length (l_w) is measured and listed in Table 1, and Fig. 5 displays the correlation between the wake length and the velocity ratio. In this figure, three cases with the flow separation at the bottom of the bubble are plotted, and the symbols denote the measured values. Least-squares fitting methods are used to fit the measured data, and it is noted that the data for the three cases align well with the fitted straight lines, i.e.

$$l_w = C_w \frac{U_c}{U_0} + l_{w,0}, \quad (2)$$

where $l_{w,0}$ stands for the wake length of the case with no co-current. For the cases where vortices appear in the wake, i.e. $N_f = 291$, 200, and 109, the slopes are 2.35, 2.26, and 1.17 respectively. It is noticed that there is a slight change in the gradient near $U_c/U_0 = 0$ for the three values of N_f . The change is more obvious at $N_f = 200$, in which the slope at high U_c/U_0 is larger than that at low U_c/U_0 . This change might be attributed to the different tail shapes, i.e. skirts at high U_c/U_0 while dimples at low U_c/U_0 .

According to Ryskin and Leal (1984) and Blanco and Magnaudet (1995), the key condition for the separation (or vortices) behind a deformable bubble is the deformation. From Fig. 3, it is noted that

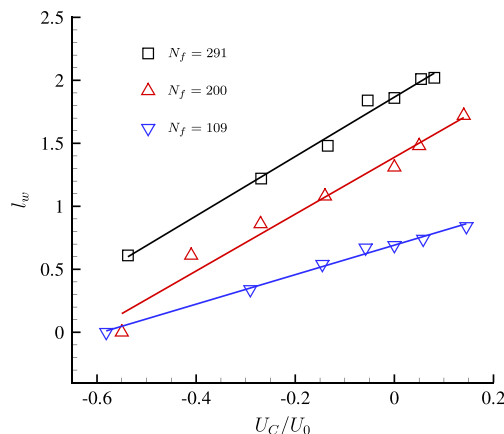


Fig. 5. Wake lengths versus flow velocity ratios. The slopes for $N_f = 291$, 200, and 109 are 2.35, 2.26, and 1.17, respectively.

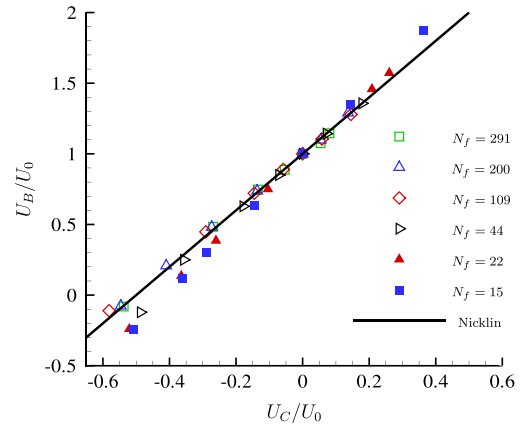


Fig. 6. Velocity correlation of a rising Taylor bubble in co-current flows.

for $N_f = 22$, the tail of bubble deforms much less than the other three cases with larger N_f , and the tail is almost spherical $U_c/U_0 = 0.52$. It is also similar for the other two cases with smaller N_f , i.e. $N_f = 44$ and 16 (listed in Table 1), and thus there is no separation observed for these three cases. The reduction of Reynolds number (Re_{U_B}) is also a factor for the wake length changes as the Reynolds number indicates the relative importance of convection and diffusion in the transport of vorticity (Ryskin and Leal, 1984). In the study of a gas bubble in an axisymmetric shear flows by Takagi et al. (1994), it is also found that the standing vortex behind the bubble is affected by the co-current flow.

As it is noticed from Table 1, the terminal velocity of the bubble in co-currents decreases with U_c/U_0 . Fig. 6 displays the correlations for U_B/U_0 and U_c/U_0 , where symbols are the simulation results, and the thick solid line denotes the prediction by Nicklin et al. (1962) with $C = 2$. The simulated coefficient, i.e. C_s , is very near to the previous predictions for $N_f \geq 44$, however for the two most viscous cases, i.e. $N_f = 22$ and 16, the simulated coefficients are 2.32 and 2.43 with the relative errors of 16% and 22%, respectively. We believe that the viscous force accounts for larger C .

3.2. Velocity distribution and shear stresses

In the previous sections, the effects of the co-current on the wake and the bubble shape including the nose and the tail are discussed. In this section, the effects on the velocity distribution along the radial direction and the shear stresses along the wall shall be discussed.

Fig. 7 shows co-current effects on the velocity distribution at $z/R_0 = -2.5$ (where the thin film has been established for most of the cases) from the bubble nose for $N_f = 200$ and 22. On the left-hand side the velocities both inside the bubble and in the thin film are displayed, while on the right-hand side, enlarged views of the velocity in the thin film regions are depicted. The disconnection points of the lines are the approximate positions where the interface is located. The symbols are simulation results, while the lines are curve fitted by a second-order polynomial least-squares fitting method. To clearly examine the co-current effects on the fluid field, the velocity shown here is the axial velocity (u_z) subtracted by the co-current velocity (u_z^{inlet}) and non-dimensionalized by \sqrt{gD} , i.e. $\frac{u_z - u_z^{inlet}}{\sqrt{gD}}$. It can be seen that the velocities both inside the bubble and in the thin film region can be best approximated by a parabolic distribution, which is similar to a pressure-driven Poiseuille flow. The parabolic distribution of the velocity in the thin film was reported previously by experimental measurements (Nogueira et al., 2006b). For the two different viscosity cases, with the

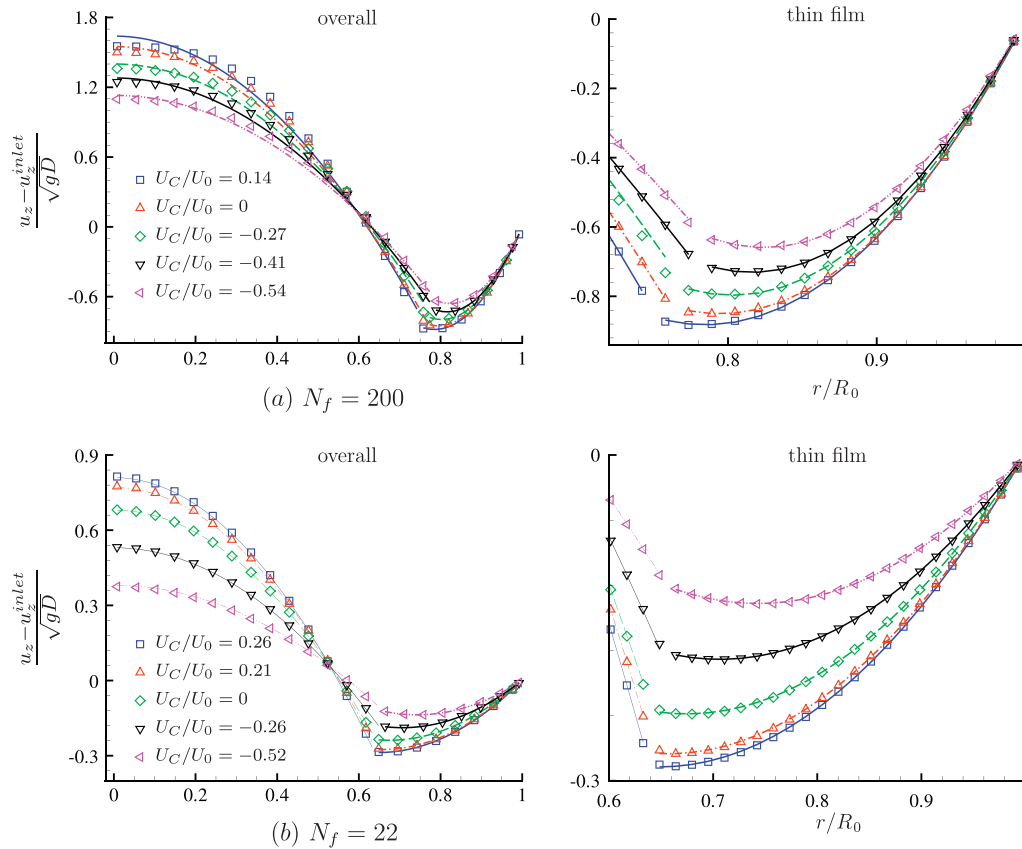


Fig. 7. Effects of the co-current on the axial velocity distributions at $z/R_0 = -2.5$ for cases with N_f of 200 and 22. The laboratory reference frame is used.

increase of the velocity ratio, the velocity $\left(\frac{u_z - u_z^{\text{inlet}}}{\sqrt{gD}}\right)$ inside the bubble also ascends, while the velocity inside the thin film reduces. These results indicate that the velocity field for the Taylor bubble rising in co-current systems is simply not the superposition of the velocity fields of the Taylor bubble rising in stagnant fluids and the co-current. From the enlarged view of the velocity in the thin film region, it is observed that the velocity gradients across the interface are different. Here, the continuity of shear stresses across the interface is used to explain:

$$\mu_b \left(\frac{\partial u_r}{\partial r} \right)_b = \mu_s \left(\frac{\partial u_r}{\partial r} \right)_s, \quad (3)$$

and then

$$\left(\frac{\partial u_r}{\partial r} \right)_b / \left(\frac{\partial u_r}{\partial r} \right)_s = \lambda. \quad (4)$$

In all the simulations, $\lambda = 100$, and thus the velocity gradients should be different by 100 times across the interface. However, it should be noted that in the front tracking method, the fluids properties including the viscosity and density are smoothed across a interfacial region with a finite thickness on the order of grid sizes, it is a challenge for this scheme to have the exact jump in the velocity gradients.

The understanding of distribution and the maximum of the wall shear stresses is of importance to investigate cell mechanics and cellular functions in many tissues and cardiovascular systems (Traub and Berk, 1998). Albuquerque et al. (2000) reported that shear stresses enhance endothelial cell repair, while Hua et al. (1993) pointed out that cells can be damaged by the forces in the

bulk liquid phase. Gas embolism, a pathological condition caused by gas bubbles in a vascular system, can occur in surgeries and in diving, and it can be a serious matter if the bubble is large.

Fig. 8 shows the shear stress distributions along the tube wall for $N_f = 291, 200, 109$, and 22. The wall shear stresses are subtracted by the shear stresses on the wall due to the co-current flow alone and are non-dimensionalized by the static pressure based on the tube diameter and suspending fluid density, i.e. $\frac{\tau_w - \tau_{wC}}{\rho_s g D}$. The wall shear stress by the co-current flow is a constant for each case, i.e.

$$\tau_{wC} = \frac{2\mu_s U_C}{R_0}. \quad (5)$$

Therefore, The shear stress distribution shown in the figure is mainly caused by buoyancy forces and the influences from the co-currents. The plots are arranged in such a way that the nose of the Taylor bubble are located near $z/R_0 = 0$. Due to the non-linearity of the problem, especially the convection terms and interfacial forces, the shear stresses for different velocity ratio are expected not the same, which is clearly demonstrated in the figure. For all the cases, the shear stresses increase from the nose and reach to their maximums at the middle, and then start to decrease from positions near the tail, and finally become zero. For $N_f = 291$ and 200, except for the smallest U_C/U_0 , the shear stresses in the middle part of the bubble continuously increase, and although the maximums decrease for all the case, the variations are small. For the smallest U_C/U_0 , the shear stresses in the middle section do not vary very much. The shear stresses of $N_f = 200$ and $U_C/U_0 = 0.14$ are wavy near the tail region, and this further demonstrates the oscillation of the bubble tail. For $N_f = 109$ and 22, the shear stresses near the middle section of the bubble are almost a

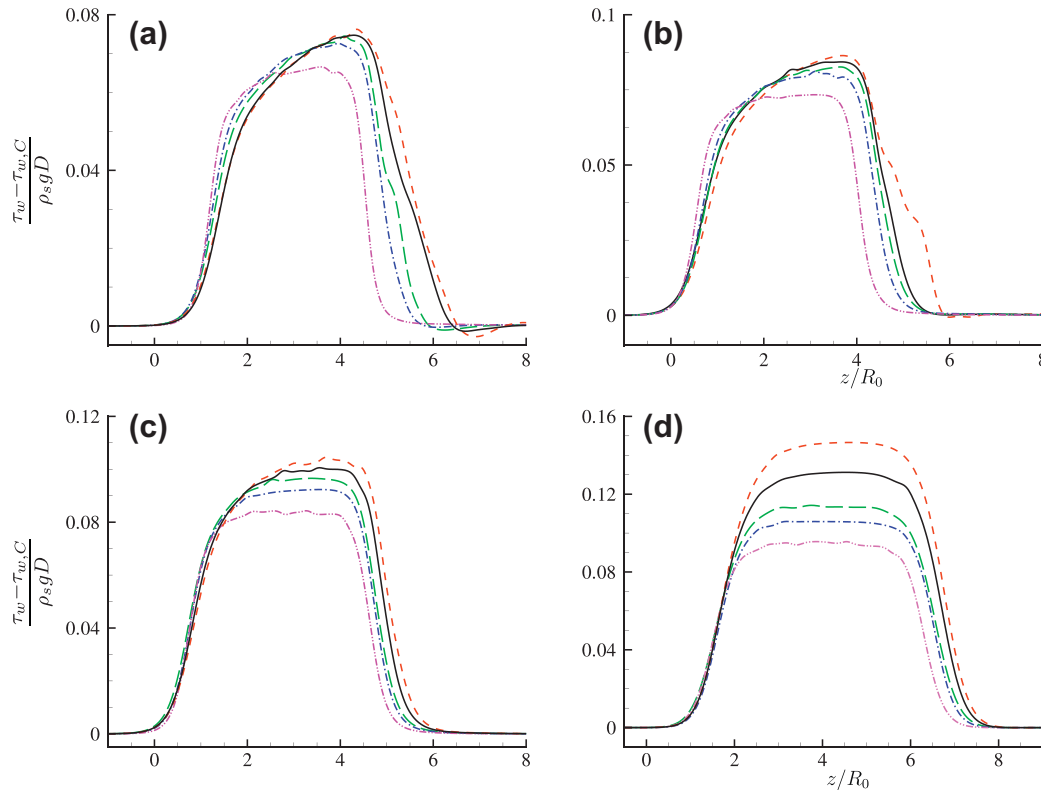


Fig. 8. Wall shear stress distribution for cases (a) $N_f = 291$, (b) $N_f = 200$, (c) $N_f = 109$, (d) $N_f = 22$. The dashed, solid, long-dash, dash-dot, and dash-dot-dot lines represent U_c/U_0 of (a) 0.081, 0, -0.13, -0.27, and -0.54, (b) 0.14, 0, -0.27, -0.41, and -0.55, (c) 0.15, 0, -0.15, -0.29, and -0.58, (d) 0.26, 0, -0.26, -0.36, and -0.52, respectively.

constant for all velocity ratios, however, comparing these two cases, the distributions of $N_f = 22$ are flatter than the ones of $N_f = 109$.

For all the cases, the maximums of the shear stresses $\left(\frac{\tau_w - \tau_{w,c}}{\rho_s g D}\right)$ reduce with the decrease of the U_c/U_0 . However, it is found the maximum shear stress actually acting on the tube wall does not vary very much with the velocity ratio, and the largest variation is less than 6%. To explain this phenomenon, the velocity field at $z/R_0 = 2.5$ of the Taylor bubble with $N_f = 22$ is shown in Fig. 9, and it should be noted that compared to the velocity displayed in Fig. 7 where the co-current velocity is subtracted (i.e. $u_z - u_c$), here the non-dimensional u_z at the lab reference frame is shown. The velocity inside the bubble especially near the rising axis is dramati-

cally affected by the co-current, while the co-current does not significantly affect the velocity inside the thin film ($r/R_0 > 0.65$). The inset of the figure displays the velocities near the wall ($r/R_0 = 1$ denotes the wall), and it is found that the difference is minimal, which leads to the small variation in the maximal wall shear stresses. Therefore, if the shear stress by a bubble rising is intended to help the cell repair or is used to clean of the inner surfaces, the co-current opposite to the buoyancy might be suggested as the duration time of shear stress on the wall is longer due to the slower motion of the bubble. However, if the bubble is dangerous, and quick removal of the bubble is needed, then the co-current in the same direction of the buoyancy force might be considered as the co-current increased the speed of the bubble motion while the maximum of the shear stress on the wall is almost unchanged.

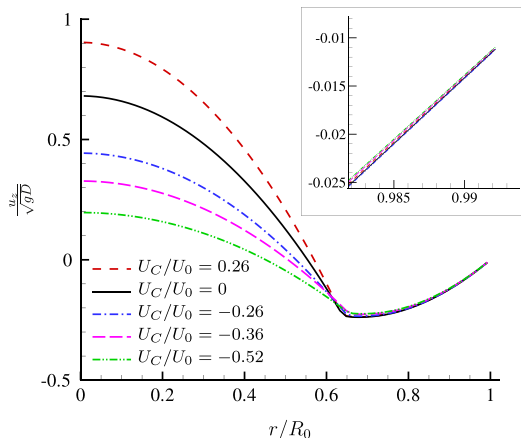


Fig. 9. Velocity distribution at $z/R_0 = 2.5$ of $N_f = 22$ at the laboratory reference frame. The inset shows an enlarged view of the velocity near the tube wall.

4. Conclusions

In this paper, numerical investigation of the co-current effects on a rising Taylor is performed, where the co-current either flows the same direction as the buoyancy force or moves in the opposite direction of the buoyancy force. The front tracking method coupled with the finite difference scheme is employed as this method has been extensively validated for bubble rising by buoyancy forces. The inverse viscosity numbers (N_f) of the Taylor bubble are $16 \leq N_f \leq 291$, which corresponds to the Archimedes number between 2×10^2 and 8×10^4 . The velocity ratios (U_c/U_0) between the mean velocity of the co-current and the bubble rising velocity in an initially stagnant liquid are in the range of $-0.52 \leq U_c/U_0 \leq 0.36$. The simulations demonstrate that the co-current affects the bubble dynamics in significant way. The upward co-current, i.e. $U_c/U_0 < 0$, elongates the bubble and the bubble skirted tail, makes the nose of the bubble sharper and the bubble slimmer, while the downward co-current shortens the bubble and the bubble tail,

makes the bubble nose blunter and bubble fatter. The upward co-current tends to promote the flow separation at the bubble bottom while the downward co-current tends to suppress the separation. Although the velocity field is not a simple superposition of the co-current and the flow field of the Taylor bubble rising in the initially stagnant liquid, the terminal velocity and the wake length are linearly depended on the corresponding variables in the stagnant fluids. The co-current affects the velocity distribution of the Taylor bubble in a very noticeable way; however, it is found that the maximal shear stresses on the tube wall do not vary much with the velocity ratios. The numerical findings on the wall shear stresses could be of help in understanding the related bio-fluids such as blood flows.

Acknowledgements

The author thanks the two reviewers for their valuable suggestions and comments for improving the quality of this article.

References

- Akbar, M.K., Ghiaasiaan, S.M., 2006. Simulation of Taylor flow in capillaries based on the volume-of-fluid technique. *Ind. Eng. Chem. Res.* 45, 5396–5403.
- Albuquerque, M.L.C., Waters, C.M., Savla, U., Schnaper, H.W., Flozak, A.S., 2000. Shear stress enhances human endothelial cell wound closure in vitro. *Am. J. Physiol. – Heart Circul. Physiol.* 279, 293–302.
- Bell, J.B., Marcus, D.L., 1992. A second-order projection method for variable density flows. *J. Comput. Phys.* 101, 334–348.
- Bendiksen, K.H., 1985. On the motion of long bubbles in vertical tubes. *Int. J. Multiph. Flow* 11, 797–812.
- Blanco, A., Magnaudet, J., 1995. The structure of the axisymmetric high-Reynolds around an ellipsoidal bubble of fixed shape number flow. *Phys. Fluids* 7, 1265–1274.
- Bugg, J.D., Saad, G.A., 2002. The velocity field around a Taylor bubble rising in a stagnant viscous fluid: numerical and experimental results. *Int. J. Multiph. Flow* 28, 791–803.
- Bugg, J.D., Mack, K., Rezkallah, K.S., 1998. A numerical model of Taylor bubbles rising through stagnant liquids in vertical tubes. *Int. J. Multiph. Flow* 24, 271–281.
- Campos, J.B.L.M., Guedes de Carvalho, J.R.F., 1988. An experimental study of the wake of gas slugs rising in liquids. *J. Fluid Mech.* 196, 27–37.
- Chen, L., Garimella, S.V., Reizes, J.A., Leonardi, E., 1999. The development of a bubble rising in a viscous fluid. *J. Fluid Mech.* 387, 61–96.
- Clift, R., Grace, J.R., Weber, M.E., 1978. *Bubbles, Drops, and Particles*. Academic Press, Inc., New York.
- Collins, R., Moraes, F.F.D., Davidson, J.F., Harrison, D., 1978. The motion of a large gas bubble rising through liquid flowing in a tube. *J. Fluid Mech.* 89, 497–514.
- Davies, R.M., Taylor, G.I., 1950. The mechanics of large bubbles rising through liquids in tubes. *Proc. Roy. Soc. Lond. A* 200, 375–390.
- Dumitrescu, D.T., 1943. Stromung an einer Luftblase im senkrechten Rohr. *Z. Angew. Math. Mech.* 23, 139–149.
- Esmaeeli, A., Tryggvason, G., 1998. Direct numerical simulations of bubbly flows. Part 1. Low Reynolds number arrays. *J. Fluid Mech.* 377, 313–345.
- Esmaeeli, A., Tryggvason, G., 1999. Direct numerical simulations of bubbly flows. Part 2. Moderate Reynolds number arrays. *J. Fluid Mech.* 385, 325–358.
- Esmaeeli, A., Tryggvason, G., 2005. A direct numerical simulation study of the buoyant rise of bubbles at $O(100)$ Reynolds number. *Phys. Fluids* 17, 093303.
- Fabre, J., Liné, A., 1992. Modelling of two-phase slug flow. *Annu. Rev. Fluid Mech.* 24, 21–46.
- Feng, J.Q., 2009. A long gas bubble moving in a tube with flowing liquid. *Int. J. Multiph. Flow* 35, 738–746.
- Grace, J.R., Clift, R., 1979. Dependence of slug rise velocity on tube Reynolds number in vertical gas–liquid flow. *Chem. Eng. Sci.* 34, 1348–1350.
- Griffith, B.E., Peskin, C.S., 2005. On the order of accuracy of the immersed boundary method: higher order convergence rates for sufficiently smooth problems. *J. Comput. Phys.* 208, 75–105.
- Gunsing, M., 2004. *Modelling Bubbly Flows Using Volume of Fluid, Front Tracking and Discrete Bubble Models*. Ph.D. Thesis, University of Twente, The Netherlands.
- Hua, J.M., Erickson, L.E., Yiin, T.Y., Glasgow, L.A., 1993. A review of the effects of shear and interfacial phenomena on cell viability. *Crit. Rev. Biotechnol.* 13, 305–328.
- Kang, C.W., Quan, S.P., Lou, J., 2010. Numerical studies of bubble necking in viscous liquids. *Phys. Rev. E* 77, 066303.
- Lu, X., Prosperetti, A., 2009. A numerical study of Taylor bubbles. *Ind. Eng. Chem. Res.* 48, 242–252.
- Mandal, T.K., Das, G., Das, P.K., 2007. Prediction of rise velocity of a liquid Taylor bubble in a vertical tube. *Phys. Fluids* 19, 128109:1–128109:4.
- Mao, Z.S., Dukler, A.E., 1991. The motion of Taylor bubbles in vertical tubes: II. Experimental data and simulations for laminar and turbulent flow. *Chem. Eng. Sci.* 46, 2055–2064.
- Mukundakrishnan, K., Quan, S.P., Eckmann, D.M., Ayyaswamy, P.S., 2007. Numerical study of wall effects on buoyant gas-bubble rise in a liquid-filled finite cylinder. *Phys. Rev. E* 76, 036308:1–036308:15.
- Ndinisa, N.V., Wiley, D.E., Fletcher, D.F., 2005. Computational fluid dynamics simulations of Taylor bubbles in tubular membranes: model validation and application to laminar flow systems. *Chem. Eng. Res. Des.* 83, 40–49.
- Nicklin, D.J., Wilkes, J.O., Davidson, J.F., 1962. Two-phase flow in vertical tubes. *Trans. Inst. Chem. Eng.* 40, 61–68.
- Nogueira, S., Riethmuller, M.L., Campos, J.B.L.M., Pinto, A.M.F.R., 2006a. Flow in the nose region and annular film around a Taylor bubble rising through vertical columns of stagnant and flowing newtonian liquids. *Chem. Eng. Sci.* 61, 845–857.
- Nogueira, S., Riethmuller, M.L., Campos, J.B.L.M., Pinto, A.M.F.R., 2006b. Flow patterns in the wake of a Taylor bubble rising through vertical columns of stagnant and flowing newtonian liquids: an experimental study. *Chem. Eng. Sci.* 61, 7199–7212.
- Pinto, A.M.F.R., Coelho Pinheiro, M.N., Nogueira, S., Ferreira, V.D., Campos, J.B.L.M., 2000. Experimental study on the transition in the velocity of individual Taylor bubbles in vertical upward co-current liquid flow. *Chem. Eng. Res. Des.* 78, 1139–1146.
- Polonsky, S., Shemer, L., Barnea, D., 1999. The relation between the Taylor bubble motion and the velocity field ahead of it. *Int. J. Multiph. Flow* 25, 957–975.
- Prosperetti, A., Tryggvason, G., 2007. *Computational Methods for Multiphase Flow*. Cambridge University Press.
- Ryskin, G., Leal, L.C., 1984. Numerical solution of free-boundary problems in fluid mechanics. Part 2. Buoyancy-driven motion of a gas bubble through a quiescent liquid. *J. Fluid Mech.* 148, 19–35.
- Taha, T., Cui, Z.F., 2006. CFD modelling of slug flow in vertical tubes. *Chem. Eng. Sci.* 61, 676–687.
- Takagi, S., Prosperetti, A., Matsumoto, Y., 1994. Drag coefficient of a gas bubble in an axisymmetric shear flow. *Phys. Fluids* 6, 3186–3188.
- Taylor, G.I., 1961. Deposition of a viscous fluid on the wall of a tube. *J. Fluid Mech.* 10, 161–165.
- Traub, O., Berk, B.C., 1998. Laminar shear stress – mechanisms by which endothelial cells transduce an atheroprotective force. *Arterioscler. Thromb. Vasc. Biol.* 18, 677–685.
- Tryggvason, G., Bunner, B., Esmaeeli, A., Juric, D., Al-Rawahi, N., Tauber, W., Han, J., Nas, S., Jan, Y.J., 2001. A front-tracking method for the computations of multiphase flow. *J. Comput. Phys.* 169, 708–759.
- van Hout, R., Gulitski, A., Barnea, D., Shemer, L., 2002. Experimental investigation of the velocity field induced by a Taylor bubble rising in stagnant water. *Int. J. Multiph. Flow* 28, 579–596.
- Viana, F., Pardo, R., Yanez, R., Trallero, J.L., Joseph, D.D., 2003. Universal correlation for the rise velocity of long gas bubbles in round pipes. *J. Fluid Mech.* 494, 379–398.
- Wallis, G.B., 1969. *One-Dimensional Two-phase Flow*. McGraw Hill.